electronics

MDPI

Article

Ballistic Performance of Quasi-One-Dimensional Hafnium Disulfide Field-Effect Transistors

Mislav Matić and Mirko Poljak *

Computational Nanoelectronics Group, Faculty of Electrical Engineering and Computing, University of Zagreb, HR 10000 Zagreb, Croatia; mislav.matic@fer.hr

* Correspondence: mirko.poljak@fer.hr; Tel.: +385-1-6129-924

Abstract: Hafnium disulfide (HfS_2) monolayer is one of the most promising two-dimensional (2D) materials for future nanoscale electronic devices, and patterning it into quasi-one-dimensional HfS2 nanoribbons (HfS_2NRs) enables multi-channel architectures for field-effect transistors (FETs). Electronic, transport and ballistic device characteristics are studied for sub-7 nm-wide and ~15 nm-long zigzag HfS_2NR FETs using non-equilibrium Green's functions (NEGF) formalism with density functional theory (DFT) and maximally localized Wannier functions (MLWFs). We provide an in-depth analysis of quantum confinement effects on ON-state performance. We show that bandgap and hole transport mass are immune to downscaling effects, while the ON-state performance is boosted by up to 53% but only in n-type devices. Finally, we demonstrate that HfS_2NR FETs can fulfill the industry requirements for future technology nodes, which makes them a promising solution for FET architectures based on multiple nanosheets or nanowires.

Keywords: density functional theory (DFT); hafnium disulfide (HfS_2); nanoribbon; non-equilibrium Green's function (NEGF); quantum transport; quasi-one-dimensional

Citation: Matić, M.; Poljak, M. Ballistic Performance of Quasi-One-Dimensional Hafnium Disulfide Field-Effect Transistors. *Electronics* **2024**, *13*, 1048. https://doi.org/10.3390/electronics13061048

Academic Editors: Jae-Hyung Jang, Tao Wang, Frédérique Ducroquet, Yi Gu and Hongtao Li

Received: 2 February 2024
Revised: 4 March 2024
Accepted: 8 March 2024
Published: 11 March 2024

1. Introduction

Atomically thin two-dimensional (2D) materials (2DMs) have arisen as potential candidates for future transistor channel materials [1–3] since the discovery of graphene in 2004 [4]. The 2DMs exhibit near-ballistic transport properties and show potential for future high-performance electronic devices due to atomic thickness and dangling-bond-free surfaces [5]. Despite their promising characteristics, the 2DM devices are severely limited by the high contact resistance that degrades the device performance [6–8]. After graphene, more than 1800 2DMs have been predicted to be stable [9], and many of them have shown promise as channel material with transition metal dichalcogenides (TMDs), such as MoS_2, $MoTe_2$, WS_2, WSe_2, SnS_2, etc. [10–12], being among the most promising for future FETs. One hundred 2DMs were studied recently in [13] for future logic devices where monolayer hafnium disulfide (HfS_2) is reported to be one of the best-performing 2DMs for future ultra-scaled FETs due to a combination of electronic and transport properties such as low effective mass and high injection velocity that result in high ON-state current for both n- and p-FETs. The electronic, transport, and device properties of 2D HfS_2 were studied in detail in [13–15] by advanced theoretical calculations, whereas experimental work on few-layer HfS_2 FETs was reported in [16,17] where integration compatibility of monolayer HfS_2 with HfO_2 high-*k* dielectric was emphasized as one the biggest strengths of realization of devices with HfS_2.

With current state-of-the-art multi-bridge channel (MBC) FETs with silicon nanosheets or nanowires gaining momentum in the industry, 2DMs patterned into quasi-one-dimensional (quasi-1D) structures such as nanoribbons could replace silicon and extend Moore's law by offering higher integration density [18–20]. Additionally, quantum confinement effects provide avenues for tuning the material properties, which could benefit the performance of

such electronic nanodevices. Recently, various nanoribbons with ultimately downscaled widths were experimentally reported, including graphene nanoribbons (GNRs) [21,22] and phosphorene nanoribbons (PNRs) [23,24], which affirms the possibility of constructing MBC FETs, at least in principle, with quasi-1D 2DM nanostructures. Therefore, given the promising performance of 2D HfS_2 FETs, it is imperative to systematically explore the electronic, transport, and device properties of quasi-1D nanoribbons of HfS_2 (HfS_2NRs) about which nothing is currently known in the literature.

In this paper, we present an ab initio study on HfS_2NRs using density functional theory (DFT) to obtain the electronic structure, and maximally localized Wannier functions (MLWFs) to transform DFT Hamiltonians into localized basis suitable for quantum transport simulation. The MLWF Hamiltonians are then coupled to our in-house non-equilibrium Green's function (NEGF)-based quantum transport [25,26] solver to obtain the relevant properties of HfS_2NRs and HfS_2NR FETs. Most importantly, we report the degradation of pFET performance while scaling down the nanoribbon width; however, the driving current in HfS_2NR nFETs is surprisingly boosted in ~2 nm-wide transistors by the quantum confinement effects. These findings are further explained by investigating the bandgap, density of states and carriers, current density, and injection velocity. Finally, we compare HfS_2NR n- and p-type FETs to other 2DMs and to the requirements set in the International Roadmap for Devices and Systems (IRDS). We show that both n- and p-type HfS_2NR FETs with nanoribbon widths in the range from ≈2 nm to ≈5 nm can fulfil the goals set for future logic devices.

2. Methods

The unit cell of monolayer HfS_2 (Figure 1a) is obtained from the Materials Cloud [27] and scaled to construct the supercells of zigzag HfS_2 nanoribbons with hydrogen-passivated edges. The nanoribbon structure from the top and side views is shown in Figures 1b and 1c, respectively. The zigzag direction exhibits the highest curvature of the dominant subbands in the valence and conduction bands, which hints at excellent carrier transport in these devices. The HfS_2NR supercells are constructed with respect to the number of HfS_2 unit cells repeated along the nanoribbon width (W). This number ranges from 2 to 10 unit cells, which corresponds to W from 1.36 nm to 6.39 nm. After defining the initial structure, we employ an ab initio plane-wave DFT, implemented in the Quantum Espresso (QE) program package (v.6.8) [28], to relax the nanoribbon structure and obtain the Hamiltonians. A 20 Å vacuum is added in confined directions to exclude any interactions between layers. The DFT calculations use Perdew–Burke–Ernzerhof generalized gradient approximation (PBE-GGA) [29] as the exchange–correlation functional with plane augmented wave (PAW) pseudopotentials. The Brillouin zone is sampled with $1 \times 15 \times 1$ Monkhorst–Pack k-point grid [30] where 15 k-points are in transport direction, and the cutoff energy is set to 1360 eV. Convergence thresholds for ionic forces are fixed to 10^{-3} eV/Å, while 10^{-4} eV is used for total energy.

Energy-localized plane-wave Hamiltonians from QE are then converted into a space-localized basis using MLWFs [31] implemented in the Wannier90 (v.3.1.0) program package [32,33]. The main input into the Wannier90 tool are the trial orbitals that are used for Wannier transformation, and here we use d orbitals for Hf atoms and p orbitals for S atoms. The band structure calculated with MLWF and DFT Hamiltonians shows good agreement in the relevant energy region around the bandgap, as seen in Figure 1d that reports the dispersion of the 3.25 nm wide HfS_2NR. Finally, the supercell MLWF Hamiltonian matrices are upscaled to construct the total HfS_2NR Hamiltonian, where the ~15 nm-long nanoribbon represents the channel of the HfS_2NR FET.

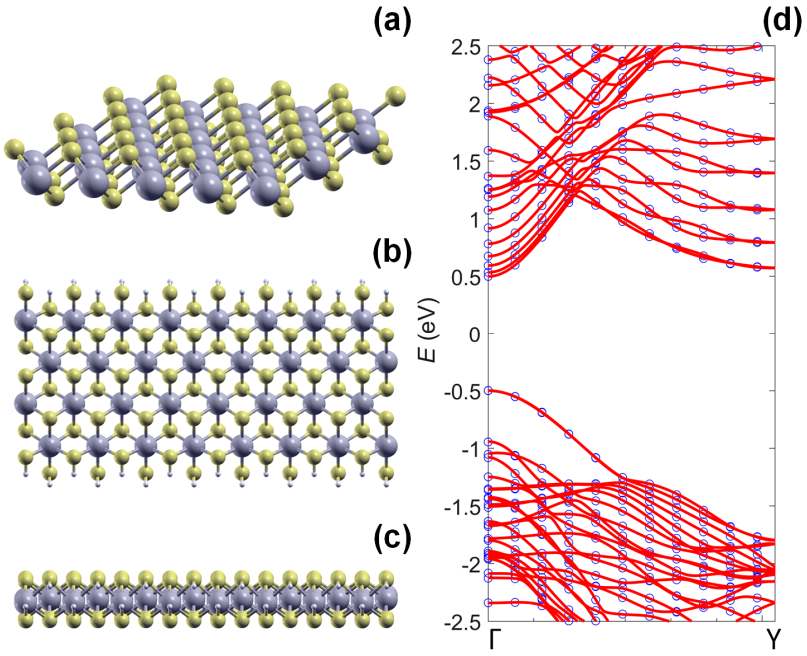

Figure 1. Illustration of (**a**) HfS_2 monolayer. (**b**) Top and (**c**) side view of the monolayer HfS_2 nanoribbon with zigzag edges. (**d**) Band structure obtained from DFT (blue dots) and MLWF (red lines).

Being primarily interested in the ON-state performance, we use the top-of-the-barrier (ToB) ballistic FET model [34] to simulate single gate n- and p-type FETs with HfS_2NR channel. Within the ToB model, only the thermionic current is calculated, which is reasonable because the assumed 15 nm long channel is long enough for negligible tunnelling. The main inputs of the ToB FET model are transmission and density of states (DOS) calculated using the NEGF formalism implemented in our in-house code [35,36]. Within NEGF, the channel is described with the total HfS_2NR Hamiltonian and source/drain (S/D) contacts are described with S/D self-energy matrices calculated using the numerically efficient Sancho–Rubio method [37,38]. The n- and p-type FETs with zigzag HfS_2NR channels are simulated with ideal electrostatic control by the gate, resulting in a perfect subthreshold slope, equivalent oxide thickness (EOT) of 1 nm, S/D doping set at 0.01 areal molar fraction or $\approx 2.7 \times 10^{13}$ cm^{-2}, and supply voltage (V_{DD}) set to 0.7 V. To provide a meaningful comparison between various HfS_2NR devices, simulations are performed with a common OFF-state current (I_{OFF}) set to 10 nA/µm as defined by IRDS for high performance (HP) devices [39].The setting of I_{OFF} is performed by adjusting the gate work function for each device automatically within our code. The ballistic ON-state current (I_{ON}) and the ON-state charge density at ToB are extracted when both gate and drain are biased at the supply voltage. Finally, we set EOT to 0.6 nm and compare I_{ON} and injection velocity to our previous work on GeS nanoribbon devices, in addition to one hundred 2DMs reported in [13].

3. Results and Discussion

Band structure of HfS_2NRs with various widths is reported in Figure 2a–d. All HfS_2NRs exhibit a direct bandgap at the Γ point and we observe an immunity of bandgap (E_g) to width scaling. The bandgap keeps a constant value of ≈1 eV in all nanoribbons, as reported in Figure 2e, which is slightly smaller than the 1.3 eV reported in [13] for the HfS_2 monolayer. As W is scaled down, the conduction band (CB) exhibits fewer bands near the CB minimum (CBM), while the dominant subband qualitatively remains the same. On the other hand, two degenerate subbands are visible in the valence band (VB) of wide HfS_2NRs with $W > 4$ nm, and this degeneracy is broken in narrower nanoribbons

due to strong quantum confinement effect. Namely, two-hole subbands separate and this separation increases with *W* downscaling, which is followed by an increase in the curvature of the second subband near the VB maximum (VBM). To further investigate the quantum confinement effects on the band structure of all HfS_2NR widths, we extract the electron and hole–band structure effective mass of the dominant subband, closest to the CBM or VBM, from the band structure by fitting its curvature with a parabolic approximation (Figure 2f). Electron effective mass (m_e*) is immune to scaling with $m_e^* \approx 0.2m_0$ for all nanoribbon widths. In contrast, hole effective mass (m_h*) experiences a significant width-scaling effect. Namely, m_h^* is $\approx 0.37m_0$ for HfS_2NRs with $W \geq 3.25$ nm; while scaling down the width linearly decreases m_h^* to $0.33m_0$ when $W = 1.36$ nm. Considering only the observed differences in CB and VB, where the m_h^* of the dominant (highest) subband is at least 1.6 × lower than the m_e^* for all observed HfS_2NRs, we expect a considerable difference in the performance of n- and p-FETs with HfS_2NR channels. However, this metric does not take into account degeneracy in VB or the higher number of subbands near CBM in wider nanoribbons.

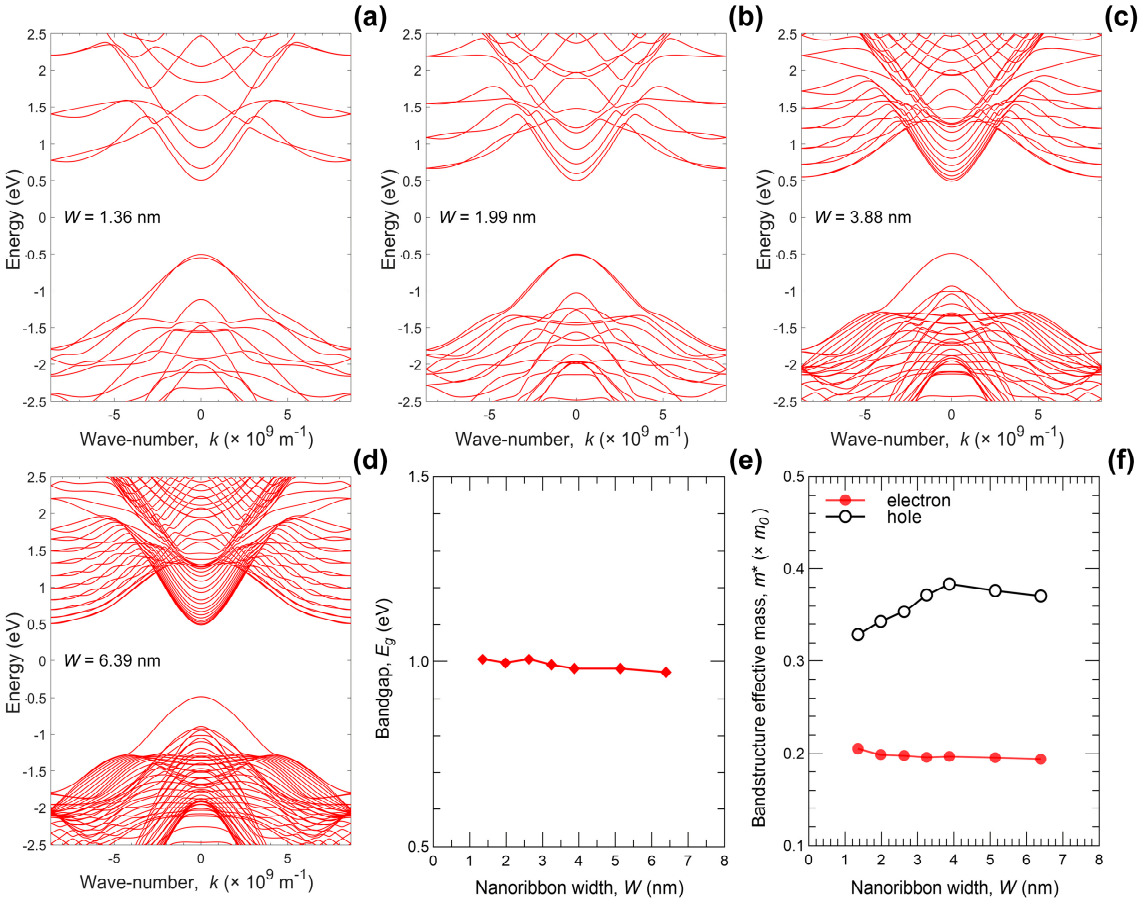

Figure 2. Band structure of zigzag HfS_2NRs with the widths of (**a**) 1.36 nm, (**b**) 1.99 nm, (**c**) 3.88 nm and (**d**) 6.39 nm. (**e**) Impact of nanoribbon width-scaling on the bandgap of zigzag HfS_2NRs. (**f**) Electron and hole band structure effective mass dependence on nanoribbon width. Effective masses are extracted for the lowest (highest) subband in the CB (VB).

To assess the performance of n- and p-type HfS_2NR FETs in Figure 3a, we plot the nanoribbon width dependence of the width-normalized ON-state current. The HfS_2NR pFETs exhibit a monotonic I_{ON} decrease from 1.5 mA/μm to 1.12 mA/μm when the width is downscaled. The only exception is the narrowest pFET that shows a slight I_{ON} increase to 1.18 mA/μm. On the other hand, for HfS_2NR nFETs, we surprisingly observe a generally monotonic increase of I_{ON} when HfS_2NR width decreases. The ON-state performance is enhanced from 1.14 mA/μm to 1.74 mA/μm when the width is downscaled from 6.39 nm

to 1.99 nm, whereas the narrowest nanoribbon with W = 1.36 nm exhibits a slight decrease of I_{ON} to 1.66 mA/µm. Therefore, quantum confinement effects induce a current boosting of 53% for nFETs with the ≈2 nm wide HfS_2NR channel. Since the performance of HfS_2NR FETs shows no correlation to the band structure effective mass, in the following paragraphs, we explore the features of charge density, density of states, and carrier injection velocity.

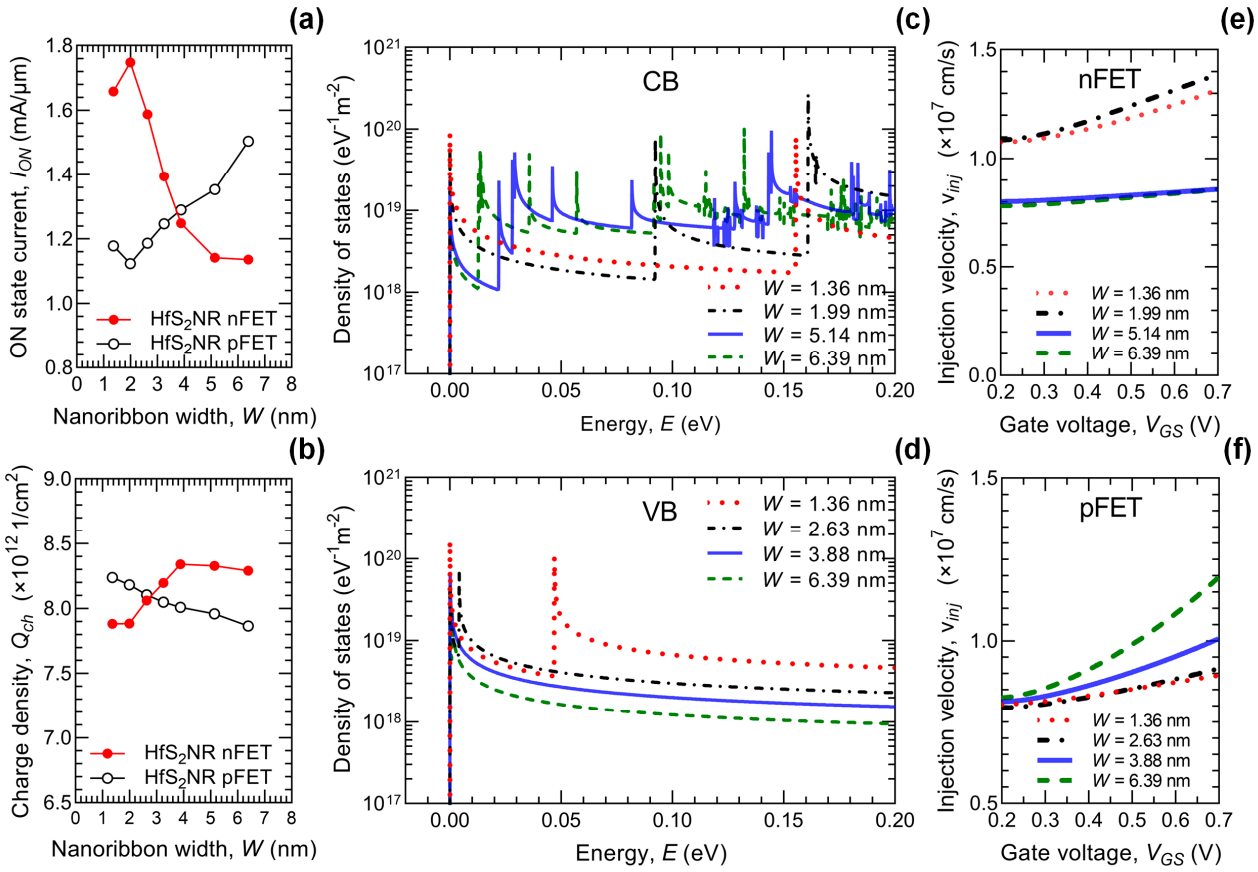

Figure 3. (**a**) ON-state current and (**b**) charge density at ToB width dependence in n- and p-type zigzag HfS_2NR FETs. I_{ON} and Q_{ch} are extracted at $V_{GS} = V_{DS} = V_{DD}$ = 0.7 V with a common I_{OFF} = 10 nA for all devices. Comparison of DOS in (**c**) conduction and (**d**) valence band of HfS_2NR FETs. All DOS and transmission plots are shifted so that the CBM and VBM are positioned at 0 eV. Dependence of injection velocity on gate voltage in (**e**) n-type and (**f**) p-type zigzag HfS_2NR FETs for various nanoribbon widths.

Charge density at the top-of-the-barrier extracted in the ON-state (Q_{CH}) for various HfS_2NR widths is plotted in Figure 3b. For HfS_2NR nFETs, we report $Q_{CH} \approx 8.3 \times 10^{12}$ cm^{-2} for $W \geq 3.88$ nm, while scaling down decreases Q_{CH} to 7.88×10^{12} cm^{-2} in the 1.36 nm wide device. On the other hand, in pFETs, charge density increases monotonically from $Q_{CH} = 7.87 \times 10^{12}$ cm^{-2} for W = 6.39 nm to $Q_{CH} = 8.24 \times 10^{12}$ cm^{-2} for W = 1.36 nm. Charge density at the top-of-the-barrier depends on DOS near the CBM or VBM. Therefore, we plot DOS near the CBM (VBM) for various HfS_2NR widths in Figure 3c,d. The HfS_2NR nFETs exhibit a dense DOS with a high number of Van Hove singularities (VHS) near the CBM. Scaling down, HfS_2NR width reduces the number of available bands in the CB, decreases the overall DOS in the 100 meV window, and, therefore, lowers the charge density in narrower HfS_2NRs. However, VB DOS that is relevant for HfS_2NR pFETs shows an increase from a single VHS to two VHSs near the VBM due to band separation of the two dominant subbands (see Figure 2a) which increases the DOS near the VBM and Q_{CH} when nanoribbon width is scaled down.

Since the trends in I_{ON} and Q_{CH} behavior, reported in Figure 3a,b, are qualitatively opposite, the only reasonable explanation for I_{ON} trends should be found in the carrier transport properties, i.e., injection velocity. Injection velocity (v_{inj}) represents the average carrier velocity at the top-of-the-barrier under the ballistic limit and it is shown in Figure 3e,f for n- and p-type HfS_2NR FETs, i.e., electrons and holes, respectively. The plots report a gate voltage (V_{GS}) dependence of v_{inj} in the range from the threshold voltage ($V_{GS} \approx 0.2$ V) to the supply voltage ($V_{GS} = 0.7$ V). The nFETs with $W \geq 5.14$ nm show almost no modulation by V_{GS} with electron v_{inj} being $\approx 0.8 \times 10^7$ cm/s. In contrast, v_{inj} increases with increasing bias in the 1.36 nm and 1.99 nm wide HfS_2NR nFETs. These two devices exhibit similar v_{inj} at the threshold voltage; however, HfS_2NR nFETs with $W = 1.99$ nm exhibit a stronger bias modulation and a higher maximum electron v_{inj} of 1.39×10^7 cm/s. The best observed v_{inj} coincides with the best reported I_{ON} in nFETs for the 1.99 nm wide HfS_2NR nFET. We attribute the optimum performance and highest electron v_{inj} for $W \approx 2$ nm to the band structure evolution, especially to the second CB subband visible in Figure 2b. Namely, for this nanoribbon, the subband crowding is not as dense as for wider HfS_2NRs, which means that higher subbands with heavier carriers do not contribute significantly to the current-carrying process. As for pFETs, hole v_{inj} at the threshold equals $\approx 0.8 \times 10^7$ cm/s for all HfS_2NR pFETs. Scaling down, HfS_2NR width decreases the strength of V_{GS} modulation of the hole v_{inj}, and devices with $W \leq 2.63$ nm show almost no bias modulation. The widest observed HfS_2NR ($W = 6.39$ nm) shows a 49% increase of hole v_{inj} to 1.2×10^7 cm/s in the ON-state. As the width is downscaled, the hole v_{inj} decreases monotonically, which agrees with the I_{ON} behavior reported in Figure 3a.

We further explore the current and transport properties in ultra-scaled HfS_2NR nanodevices by analyzing the current energy density (J_{de}) in the ON-state. The J_{de} results are shown for n- and pFETs in Figures 4a and 4b, respectively. In all devices, the current is mainly contained in the energy window up to $\approx$100 meV from the CBM/VBM. The nFETs exhibit J_{de} maximum at the CBM for the narrowest HfS_2NR, but wider HfS_2NRs exhibit a slight shift of the maximum by 20–30 meV, due to the higher number of occupied subbands. Namely, setting a common I_{OFF} for all devices results in different S/D Fermi levels (E_F) depending on device width, with a greater E_F shift upward generally observed for wider HfS_2NRs. Consequently, there are more current-carrying subbands, and the current density at the CBM is lower in wider HfS_2NR nFETs. The 1.36 nm wide HfS_2NR shows maximum current density near the CBM, with only a single dominant subband. In contrast, for $W = 1.99$ nm, the second subband carries current as well, with the second-subband current density surpassing that of the first subband above CBM + 90 meV, which leads to the maximum I_{ON} for the 2 nm wide device among all the studied HfS_2NR nFETs.

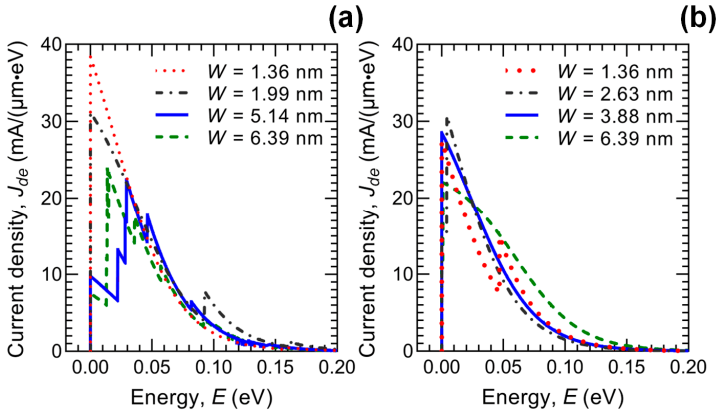

Figure 4. Current energy density at ToB in the ON-state for HfS_2NR (**a**) n-type and (**b**) p-type FETs with different nanoribbon channel widths.

In addition to the current density, band decomposed charge density (BDCD) of nanoribbons with the widths of 1.36 nm and 6.39 nm is plotted in Figures 5a and 5b, respectively.

The BDCD is shown for subbands at the CBM/VBM, along with the nearest next subbands that are denoted as next-CBM/next-VBM. Figure 5a shows that the electron current in the narrowest nanoribbon, mainly determined by the first CB subband (see Figure 4a), is distributed almost through the whole nanoribbon width, except for edge S atoms. On the other hand, electron current in the widest HfS_2NR is mostly determined by the next-CBM subband (see Figure 4a), so that the current flows away from the edges and somewhat through the middle, as shown in Figure 5b. As for HfS_2NR pFETs with current density reported in Figure 4b, J_{de} is localized near the VBM due to the dominant first subband in the VB with a considerable contribution of the second subband in some devices. The lowest two VB subbands are slightly separated, i.e., degeneracy is broken, only in the narrowest HfS_2NR (see Figure 2a), and this split results in lower transmission probability near the VBM and, therefore, lower J_{de} in pFETs with the narrowest 1.36 nm wide channel. As shown in the BDCD plots in Figure 5a,b, now addressing the situation for the VBM subband, we observe that the hole current is expected to flow exclusively along nanoribbon edges. Furthermore, for wide HfS_2NRs where two degenerate subbands are dominant near the VBM, we observe that the current flows through separate edges in VBM and next-VBM, as seen in Figure 5b, due to zero overlap between the edges. Scaling down the nanoribbon width decreases the distance between the edges, which increases the overlap of the edge states and, therefore, causes the separation of degenerate subbands near the VBM, as seen in Figure 2. Increasing the current by increasing the width would be limited due to edge transport; hence, the narrowest HfS_2NR pFETs exhibit a decreasing drive current (Figure 3a) due to higher DOS in S/D regions and related E_F downshift.

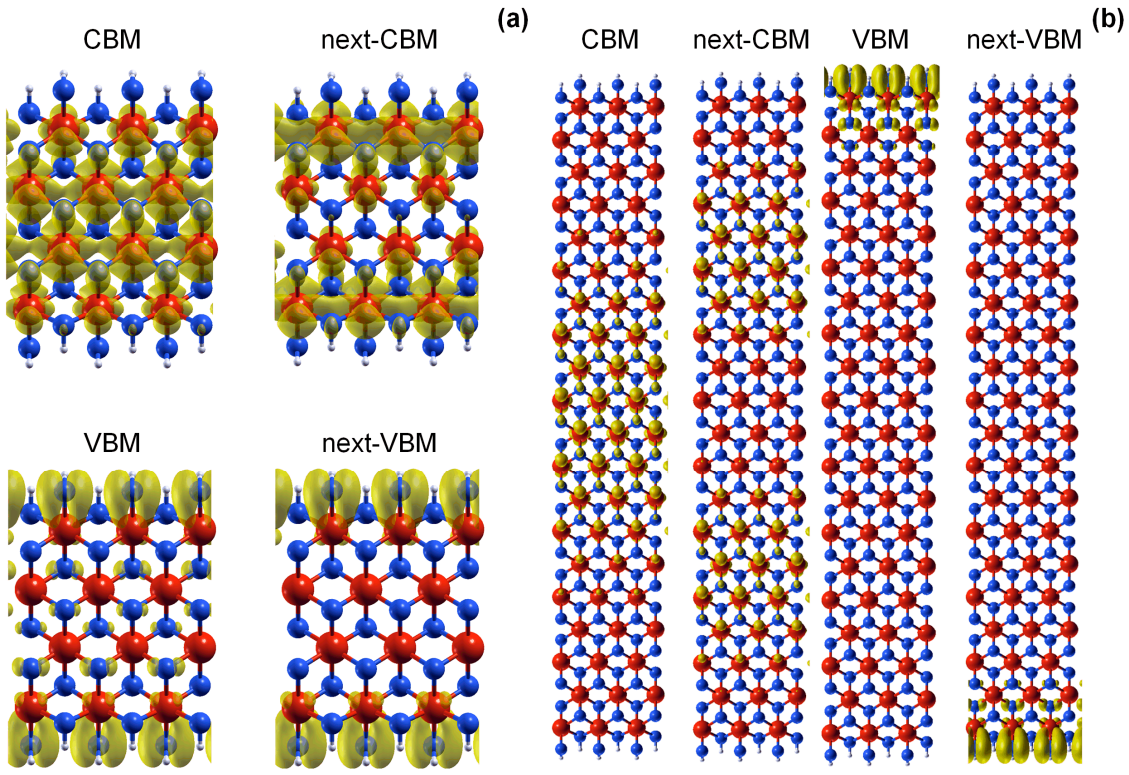

Figure 5. Band-decomposed charge density of CBM, next-CBM, VBM and next-VBM subbands of (**a**) 1.39 nm and (**b**) 6.39 nm wide HfS_2NRs. Isovalue is set at 0.001 q/bohr^3.

Finally, we compare the ON-state performance of HfS_2NR FETs with one hundred 2DMs analyzed in [13], to the armchair and zigzag GeSNRs from our previous work [36,40], and to the IRDS requirements for future logic nodes [39]. For a proper comparison with the literature data, we set the EOT to 0.6 nm (HfO_2 with ε_r = 20, t_{ox} = 3 nm) as in [13]. The injection velocity in the ON-state for nFET and pFETs is shown in Figure 6a. All HfS_2NR

n- and pFETs exhibit v_{inj} close to, or higher, than the IRDS requirement (0.9×10^7 cm/s), while achieving comparable v_{inj} values to those in 2D HfS_2 along the zigzag direction. Furthermore, only a few other large-area 2D materials such as Ge_2S_2, As_4 and P_4 exhibit higher v_{inj} compared to HfS_2NRs. This is noteworthy because HfS_2NRs are quasi-1D nanostructures with additional quantum confinement in comparison to 2DMs that are infinite 2D sheets.

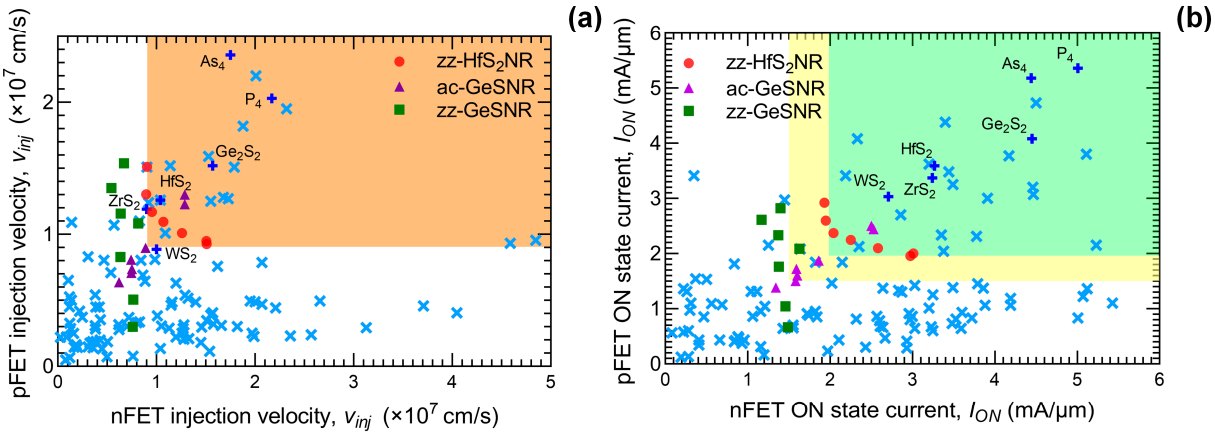

Figure 6. (**a**) nFET vs. pFET ON-state injection velocity with orange area denoting injection velocity higher than 0.9×10^7 cm/s set by IRDS 2022 for future logic nodes. (**b**) nFET vs. pFET ON-state current with a green area representing IRDS 2021 maximum I_{ON} requirement with I_{ON} = 1.979 mA/μm, and a yellow area representing the minimum I_{ON} requirement for future logic devices with I_{ON} = 1.504 mA/μm. The 100 2DMs reported in [13] are included in graphs with the most relevant materials named directly and denoted with blue plus signs, while the unnamed 2DMs are presented with light blue crosses.

The ON-state current is compared in Figure 6b again for HfS_2NR FETs from this work and one hundred 2DMs reported in [13]. We compare the data against IRDS 2021 [41] because the IRDS 2022 version, which we have used for all previous comparisons, does not provide I_{ON} requirements with zero series or contact resistance. We observe that HfS_2NR FETs exhibit a relatively high I_{ON} and all devices meet the minimum IRDS I_{ON} for both nFET and pFET devices. On the other hand, the maximum IRDS I_{ON} specification is met only by HfS_2NR FETs with W in the range from 1.99 nm to 5.14 nm. The remaining HfS_2NR FETs are close but are nevertheless beyond the edges of the acceptable I_{ON} window. Compared to the armchair and zigzag GeSNRs, only armchair GeSNRs with $W > 3$ nm show better I_{ON} performance than HfS_2NR devices in both n- and p-FET configurations. Finally, in comparison to 2D HfS_2 and other 2D materials such as WS_2, ZrS_2, Ge_2S_2, arsenene and phosphorene, all HfS_2NR FETs perform relatively poorly. Nevertheless, we stress that HfS_2NRs are quasi-1D nanostructures with strong quantum confinement effects along the width, so a direct comparison to 2D monolayers is not completely fair.

The usage of zigzag HfS_2NR for future FET architectures based on multiple parallel nanosheets or nanowires is plausible, given their fulfilment of the IRDS requirements for the ON-state current and injection velocity and, moreover, given the possibility of a matched performance of n- and p-channel devices. Although several monoelemental 2D materials and TMDs outperform hafnium disulphide nanoribbon devices, the HfS_2NR FETs still outperform most of the previously studied 2DMs when both n- and p-FET devices and their performance are considered. Meeting the IRDS requirements for the ON-state current is obtained here for the ideal single-gate FET structure, whereas the usage of multi-channel architectures such as MBC FETs could provide opportunities for further improvements in performance. Additionally, we note that this study deals with purely ballistic devices so only the upper ballistic performance limits are explored in this work, while taking into account realistic effects like carrier scattering in quasi-ballistic transport and contact

resistance would deteriorate the reported HfS_2NR FET performance. While investigating the impact of these issues is important, it is also out of the scope of the current manuscript and will be addressed in future work. Nevertheless, the potential of using ultra-scaled HfS_2NRs as a channel material in future logic devices is evident.

4. Conclusions

We present a comprehensive study on the electronic, transport and ballistic device characteristics for HfS_2 nanoribbons with a length of 15 nm and widths under 7 nm. We show that HfS_2NRs and HfS_2NR FETs exhibit promising transport properties and ON-state performance combined with an immunity of bandgap to nanoribbon width downscaling. Moreover, an unexpected and significant I_{ON} increase of up to 53% is observed in n-type FETs with HfS_2NR width of ≈2 nm. Concerning the industry goals for future technology nodes, we demonstrate that HfS_2NR FETs with nanoribbon widths in the range from 1.99 nm to 5.14 nm meet all IRDS requirements when EOT is set to 0.6 nm. Therefore, just like 2D HfS_2, quasi-1D nanostructures of monolayer HfS_2 present a promising candidate material system for ultra-scaled logic devices, especially for multi-channel nanosheet or nanowire nFETs, in which the ~2 nm wide HfS_2NRs could provide a significant performance boost due to the strong quantum confinement effect on the band structure.

Author Contributions: Conceptualization, M.M. and M.P.; methodology, M.M.; software, M.M.; validation, M.M. and M.P.; formal analysis, M.M. and M.P.; investigation, M.M.; resources, M.P.; data curation, M.M.; writing—original draft preparation, M.M.; writing—review and editing, M.P.; visualization, M.M.; supervision, M.P.; project administration, M.P.; funding acquisition, M.P. All authors have read and agreed to the published version of the manuscript.

Funding: This research was funded by Croatian Science Foundation under the project CONAN2D, grant number UIP-2019-04-3493.

Data Availability Statement: The data that support the findings of this study are available from the corresponding author, M.P., upon reasonable request.

Conflicts of Interest: The authors declare no conflicts of interest.

References

1. Fiori, G.; Bonaccorso, F.; Iannaccone, G.; Palacios, T.; Neumaier, D.; Seabaugh, A.; Banerjee, S.K.; Colombo, L. Electronics Based on Two-Dimensional Materials. *Nat. Nanotechnol.* **2014**, *9*, 768–779. [CrossRef] [PubMed]
2. Schwierz, F.; Pezoldt, J.; Granzner, R. Two-Dimensional Materials and Their Prospects in Transistor Electronics. *Nanoscale* **2015**, *7*, 8261–8283. [CrossRef] [PubMed]
3. Iannaccone, G.; Bonaccorso, F.; Colombo, L.; Fiori, G. Quantum Engineering of Transistors Based on 2D Materials Heterostructures. *Nat. Nanotechnol.* **2018**, *13*, 183–191. [CrossRef] [PubMed]
4. Novoselov, K.S.; Geim, A.K.; Morozov, S.V.; Jiang, D.; Zhang, Y.; Dubonos, S.V.; Grigorieva, I.V.; Firsov, A.A. Electric Field Effect in Atomically Thin Carbon Films. *Science* **2004**, *306*, 666–669. [CrossRef]
5. Zeng, S.; Tang, Z.; Liu, C.; Zhou, P. Electronics Based on Two-Dimensional Materials: Status and Outlook. *Nano Res.* **2021**, *14*, 1752–1767. [CrossRef]
6. Allain, A.; Kang, J.; Banerjee, K.; Kis, A. Electrical Contacts to Two-Dimensional Semiconductors. *Nat. Mater.* **2015**, *14*, 1195–1205. [CrossRef] [PubMed]
7. Gahoi, A.; Kataria, S.; Driussi, F.; Venica, S.; Pandey, H.; Esseni, D.; Selmi, L.; Lemme, M.C. Dependable Contact Related Parameter Extraction in Graphene–Metal Junctions. *Adv. Electron. Mater.* **2020**, *6*, 2000386. [CrossRef]
8. Poljak, M.; Matić, M.; Zeljko, A. Minimum Contact Resistance in Monoelemental 2D Material Nanodevices with Edge-Contacts. *IEEE Electron. Dev. Lett.* **2021**, *42*, 1240–1243. [CrossRef]
9. Mounet, N.; Gibertini, M.; Schwaller, P.; Campi, D.; Merkys, A.; Marrazzo, A.; Sohier, T.; Castelli, I.E.; Cepellotti, A.; Pizzi, G.; et al. Two-Dimensional Materials from High-Throughput Computational Exfoliation of Experimentally Known Compounds. *Nat. Nanotech.* **2018**, *13*, 246–252. [CrossRef]
10. Radisavljevic, B.; Radenovic, A.; Brivio, J.; Giacometti, V.; Kis, A. Single-Layer MoS_2 Transistors. *Nat. Nanotech.* **2011**, *6*, 147–150. [CrossRef]
11. Huang, Y.; Sutter, E.; Sadowski, J.T.; Cotlet, M.; Monti, O.L.A.; Racke, D.A.; Neupane, M.R.; Wickramaratne, D.; Lake, R.K.; Parkinson, B.A.; et al. Tin Disulfide—An Emerging Layered Metal Dichalcogenide Semiconductor: Materials Properties and Device Characteristics. *ACS Nano* **2014**, *8*, 10743–10755. [CrossRef]

12. Ovchinnikov, D.; Allain, A.; Huang, Y.-S.; Dumcenco, D.; Kis, A. Electrical Transport Properties of Single-Layer WS_2. *ACS Nano* **2014**, *8*, 8174–8181. [CrossRef]
13. Klinkert, C.; Szabó, Á.; Stieger, C.; Campi, D.; Marzari, N.; Luisier, M. 2-D Materials for Ultrascaled Field-Effect Transistors: One Hundred Candidates under the *Ab Initio* Microscope. *ACS Nano* **2020**, *14*, 8605–8615. [CrossRef]
14. Afzalian, A.; Pourtois, G. ATOMOS: An ATomistic MOdelling Solver for Dissipative DFT Transport in Ultra-Scaled HfS_2 and Black Phosphorus MOSFETs. In Proceedings of the 2019 International Conference on Simulation of Semiconductor Processes and Devices (SISPAD), Udine, Italy, 4–6 September 2019; IEEE: Udine, Italy, 2019; pp. 1–4.
15. Zhang, W.; Huang, Z.; Zhang, W.; Li, Y. Two-Dimensional Semiconductors with Possible High Room Temperature Mobility. *Nano Res.* **2014**, *7*, 1731–1737. [CrossRef]
16. Kanazawa, T.; Amemiya, T.; Ishikawa, A.; Upadhyaya, V.; Tsuruta, K.; Tanaka, T.; Miyamoto, Y. Few-Layer HfS2 Transistors. *Sci. Rep.* **2016**, *6*, 22277. [CrossRef]
17. Xu, K.; Huang, Y.; Chen, B.; Xia, Y.; Lei, W.; Wang, Z.; Wang, Q.; Wang, F.; Yin, L.; He, J. Toward High-Performance Top-Gate Ultrathin HfS_2 Field-Effect Transistors by Interface Engineering. *Small* **2016**, *12*, 3106–3111. [CrossRef]
18. Fiori, G.; Iannaccone, G. Simulation of Graphene Nanoribbon Field-Effect Transistors. *IEEE Electron. Device Lett.* **2007**, *28*, 760–762. [CrossRef]
19. Li, X.; Wang, X.; Zhang, L.; Lee, S.; Dai, H. Chemically Derived, Ultrasmooth Graphene Nanoribbon Semiconductors. *Science* **2008**, *319*, 1229–1232. [CrossRef] [PubMed]
20. Poljak, M.; Song, E.B.; Wang, M.; Suligoj, T.; Wang, K.L. Influence of Edge Defects, Vacancies, and Potential Fluctuations on Transport Properties of Extremely Scaled Graphene Nanoribbons. *IEEE Trans. Electron. Devices* **2012**, *59*, 3231–3238. [CrossRef]
21. Chen, C.; Lin, Y.; Zhou, W.; Gong, M.; He, Z.; Shi, F.; Li, X.; Wu, J.Z.; Lam, K.T.; Wang, J.N.; et al. Sub-10-Nm Graphene Nanoribbons with Atomically Smooth Edges from Squashed Carbon Nanotubes. *Nat. Electron.* **2021**, *4*, 653–663. [CrossRef]
22. Wang, H.S.; Chen, L.; Elibol, K.; He, L.; Wang, H.; Chen, C.; Jiang, C.; Li, C.; Wu, T.; Cong, C.X.; et al. Towards Chirality Control of Graphene Nanoribbons Embedded in Hexagonal Boron Nitride. *Nat. Mater.* **2021**, *20*, 202–207. [CrossRef] [PubMed]
23. Watts, M.C.; Picco, L.; Russell-Pavier, F.S.; Cullen, P.L.; Miller, T.S.; Bartuś, S.P.; Payton, O.D.; Skipper, N.T.; Tileli, V.; Howard, C.A. Production of Phosphorene Nanoribbons. *Nature* **2019**, *568*, 216–220. [CrossRef] [PubMed]
24. Zhang, W.; Enriquez, H.; Tong, Y.; Mayne, A.J.; Bendounan, A.; Smogunov, A.; Dappe, Y.J.; Kara, A.; Dujardin, G.; Oughaddou, H. Flat Epitaxial Quasi-1D Phosphorene Chains. *Nat. Commun.* **2021**, *12*, 5160. [CrossRef] [PubMed]
25. Datta, S. *Electronic Transport in Mesoscopic Systems*; Cambridge University Press: Cambridge, UK, 1997; ISBN 978-0-521-59943-6.
26. Poljak, M. *Kvantni Transport na Nanoskali [Quantum Transport on the Nanoscale]*, 1st ed.; Element: Zagreb, Croatia, 2023; ISBN 978-953-250-236-7.
27. Talirz, L.; Kumbhar, S.; Passaro, E.; Yakutovich, A.V.; Granata, V.; Gargiulo, F.; Borelli, M.; Uhrin, M.; Huber, S.P.; Zoupanos, S.; et al. Materials Cloud, a Platform for Open Computational Science. *Sci. Data* **2020**, *7*, 299. [CrossRef] [PubMed]
28. Giannozzi, P.; Baroni, S.; Bonini, N.; Calandra, M.; Car, R.; Cavazzoni, C.; Ceresoli, D.; Chiarotti, G.L.; Cococcioni, M.; Dabo, I.; et al. QUANTUM ESPRESSO: A Modular and Open-Source Software Project for Quantum Simulations of Materials. *J. Phys. Condens. Matter.* **2009**, *21*, 395502. [CrossRef]
29. Perdew, J.P.; Burke, K.; Ernzerhof, M. Generalized Gradient Approximation Made Simple. *Phys. Rev. Lett.* **1996**, *77*, 3865–3868. [CrossRef]
30. Monkhorst, H.J.; Pack, J.D. Special Points for Brillouin-Zone Integrations. *Phys. Rev. B* **1976**, *13*, 5188–5192. [CrossRef]
31. Marzari, N.; Vanderbilt, D. Maximally Localized Generalized Wannier Functions for Composite Energy Bands. *Phys. Rev. B* **1997**, *56*, 12847–12865. [CrossRef]
32. Pizzi, G.; Vitale, V.; Arita, R.; Blügel, S.; Freimuth, F.; Géranton, G.; Gibertini, M.; Gresch, D.; Johnson, C.; Koretsune, T.; et al. Wannier90 as a Community Code: New Features and Applications. *J. Phys. Condens. Matter* **2020**, *32*, 165902. [CrossRef]
33. Calderara, M.; Brück, S.; Pedersen, A.; Bani-Hashemian, M.H.; VandeVondele, J.; Luisier, M. Pushing Back the Limit of *Ab-Initio* Quantum Transport Simulations on Hybrid Supercomputers. In Proceedings of the International Conference for High Performance Computing, Networking, Storage and Analysis, Austin, TX, USA, 15–20 November 2015; pp. 1–12.
34. Rahman, A.; Guo, J.; Datta, S.; Lundstrom, M.S. Theory of Ballistic Nanotransistors. *IEEE Trans. Electron. Devices* **2003**, *50*, 1853–1864. [CrossRef]
35. Matić, M.; Župančić, T.; Poljak, M. Parallelized Ab Initio Quantum Transport Simulation of Nanoscale Bismuthene Devices. In Proceedings of the 2022 45th Jubilee International Convention on Information, Communication and Electronic Technology (MIPRO), Opatija, Croatia, 23–27 May 2022; pp. 118–123.
36. Matić, M.; Poljak, M. Ab Initio Quantum Transport Simulations of Monolayer GeS Nanoribbons. *Solid-State Electron.* **2022**, *197*, 108460. [CrossRef]
37. Pourfath, M. *The Non-Equilibrium Green's Function Method for Nanoscale Device Simulation*; Springer: Wien, Austria, 2014; ISBN 978-3-7091-1799-6.
38. Sancho, M.P.L.; Sancho, J.M.L.; Rubio, J. Quick Iterative Scheme for the Calculation of Transfer Matrices: Application to Mo (100). *J. Phys. F Met. Phys.* **1984**, *14*, 1205–1215. [CrossRef]
39. IEEE International Roadmap for Devices and Systems (IRDS), 2022 Update. Available online: https://Irds.Ieee.Org/editions/2022/more-moore (accessed on 15 January 2024).

40. Matić, M.; Poljak, M. Electronic, Transport and Ballistic Device Properties of Quasi-One-Dimensional GeS. *J. Comput. Electron.* **2023**, *22*, 1350–1362. [CrossRef]
41. IEEE International Roadmap for Devices and Systems (IRDS), 2021 Update. Available online: https://Irds.Ieee.Org/editions/2021/more-moore (accessed on 17 January 2024).